

1 **Testing ground based observations of wave activity in the (lower and upper) atmosphere**
2 **as possible (complementary) indicators of streamer events**

3 **Michal Kozubek**¹, Lisa Kuchelbacher², Jaroslav Chum¹, Tereza Sindelarova¹, Franziska
4 Trinkl^{2, a}, Katerina Podolska¹

5 ¹Institute of Atmospheric Physics CAS, Bocni II 1401, Prague, 14100, Czech Republic

6 ² Earth Observation Center, Deutsches Zentrum für Luft- und Raumfahrt, 82234 Weßling,
7 Germany

8 ^a now at Karlsruhe Institute of Technology (KIT), Institute of Meteorology and Climate
9 Research, Karlsruhe, Germany

10 **Correspondence: Michal Kozubek, kom@ufa.cas.cz**

11 **Keywords:** gravity waves, streamer events, infrasound, Doppler measurements

12
13 **Abstract:** For a better understanding of atmospheric dynamics, it is very important to know
14 the general conditions (dynamics and chemistry) of the atmosphere. Planetary waves (PWs)
15 are global scale waves, which are well-known as main drivers of the large-scale weather
16 patterns in mid-latitudes on time scales from several days up to weeks in the troposphere.
17 When PWs break, they often cut pressure cells off the jet stream. A specific example are so-
18 called streamer events, which occur predominantly in the lower stratosphere at mid- and high-
19 latitudes. For streamer events we check, whether there are any changes in gravity wave (GW)
20 or infrasound characteristics related to these events in ionospheric and surface measurements
21 (continuous Doppler soundings, two arrays of microbarometers) in the Czech Republic.

22 Phenomena in infrasound arrival parameters undoubtedly related to streamer events were not
23 identified in observations of two stations located in Central Europe. Simulations of infrasound
24 propagation show influences of the streamer events on the waveguide formed near the
25 tropopause. Microbarom propagation is influenced by the tropopause waveguide in a limited
26 azimuth sector and at limited distances. Due to the typical occurrence of the streamer events
27 over the North Atlantic, infrasound stations in Western Europe can be of particular interest for
28 future studies of streamer event signatures in infrasound arrivals. Arrivals to Central Europe
29 are through the waveguide formed between the ground and the upper stratosphere. The upper
30 stratosphere waveguide is not influenced by the streamer events.

31 Supplementary ground-based measurements of GW using the WBCI array in the troposphere
32 showed that GW propagation azimuths were more random during streamer and streamer-like
33 events compared to those observed during calm conditions. GW propagation characteristics
34 observed in the ionosphere by continuous Doppler soundings during streamer events did not
35 differ from those expected for the given time period.

36

37 **1) Introduction**

38 For a better comprehension of climate change, how well we understand the climate system
39 in general, and the dynamics of the atmosphere in particular is fundamentally importance. The
40 dynamical processes in the atmosphere relevant in this context in the atmosphere take place
41 over a comparatively wide range of scales in space and time. They include in particular both,
42 planetary and gravity waves. Planetary waves are one of the main drivers of the extratropical
43 circulation. When they break, they lead to an irreversible exchange of air masses between the
44 equatorial and polar region due to an amplification of their amplitudes (e.g. McIntyre &
45 Palmer, 1983; Polvani & Plumb,1992). In the lower stratosphere ozone can be used as a tracer
46 for these large-scale motions, as it has a comparatively long life-time. When planetary waves
47 break, tropical air masses of low ozone concentration are mixed poleward into the
48 surrounding atmosphere high-latitude atmosphere (e.g. Leovy et al., 1985).

49 The term "streamer" lacks a precise definition, as noted by Krüger et al. (2005). They
50 discuss various aspects of streamers, including their impact on mixing and the divergent
51 definitions associated with them. Offermann et al. (1999) describe streamers as large-scale
52 tongue-like structures formed by the meridional deflection of air masses. Streamers are
53 characterized by irreversible mixing of air masses between equatorial and polar regions which
54 is why they might be linked to planetary wave breaking (Vaugh, 1993). Eyring et al. (2003)
55 give a climatology of the seasonal and geographical distribution of streamer events. They
56 show, that streamers often occur over the Northern Atlantic and can be identified by either
57 high NO₂ or low ozone concentration. This is why we identify streamers using total ozone
58 column measurements in this paper. Eyring et al. (2003) show that streamer events occur most
59 often during winter and least during July and August in the Northern Hemisphere. During a
60 streamer event the wind field changes rather strongly over a comparatively small distance.
61 Since a streamer event shows a strong wind shear at its flanks, it is expected that it excites
62 GW (e.g. Kramer et al., 2015 and 2016 or Peters et al., 2003).

63 It is well-known that enhanced wind gradients or anticyclones can lead to the
64 excitation of gravity waves (GW) in the atmosphere (e.g. Pramitha et al., 2015; Kai et al.,
65 2010; Kramer et al., 2015, 2016 and Gerlach et al., 2003). GW have typical vertical
66 wavelengths from a few 100 m to several kilometres (Wüst & Bittner, 2006), and horizontal
67 wavelengths greater than tens of km (Wüst et al., 2018); (Rauthe et al., 2006); their wind
68 fluctuations in the upper troposphere / lower stratosphere typically have maximum amplitudes
69 of 5–10 m/s at maximum (e.g., Kramer et al., 2015). These waves transport energy and
70 momentum horizontally and vertically through the atmosphere and deposit them primarily in
71 the stratosphere and mesosphere although some deposition occurs above and below this
72 height region. The propagation of GWs is strongly dependent on the wind conditions in the
73 stratosphere since the wind speed of the middle atmosphere (10–100 km) reaches its
74 maximum there. That is why monitoring waves in upper parts of the atmosphere, e.g. based
75 on Doppler observations in the ionosphere, can provide additional information about
76 stratospheric conditions (for details see Fritts and Alexander, 2003).

77 Using pressure recordings at a microbarograph array, GWs and infrasound at the ground can
78 be observed. Ground based observations of GWs at a large aperture microbarograph array are
79 utilized in the present study as an independent data source for the analysis of GW activity
80 during streamer events. Infrasound propagation is influenced by wind and temperature fields
81 in the atmosphere. Three regions play an important role in long-distance infrasound
82 propagation: (1) the lower thermosphere; (2) the stratosphere; (3) the jet stream near the
83 tropopause and inversion layers in the troposphere (Evers and Haak, 2010). Infrasound
84 observed at the ground and emitted by distant sources mostly propagates in the stratospheric
85 waveguide (Ceranna et al., 2019). The thermospheric waveguide is not as efficient as the
86 stratospheric waveguide in the long-range infrasound propagation. Besides signal loss due to
87 geometrical spreading, infrasound absorption is important in the upper atmosphere (Bittner et
88 al., 2010). Infrasound absorption is proportional to the frequency; higher frequencies,
89 particularly those above 1 Hz undergo stronger absorption in the thermosphere (Sutherland
90 and Bass, 2004). Signal attenuation is low at frequencies of the order of $10^{-3} - 10^{-2}$ Hz (Blanc,
91 1985; Georges, 1968).

92 A number of case studies have proved that stratospheric dynamics can be deduced from
93 microbarograph measurements at the ground (Assink et al., 2014; Blixt et al., 2019; Evers and
94 Siegmund, 2009; Evers et al., 2012; Garcès et al., 2004; Le Pichon and Blanc, 2005; Le
95 Pichon et al., 2006 and 2009; Smets and Evers, 2014). Streamer events are significant

96 transient disturbances to circulation patterns in the tropopause/lower stratosphere region;
97 modifications of the stratospheric waveguide can therefore be expected. A feasibility study on
98 utilisation of ground infrasound measurements in research of streamer events is performed
99 here. Its aim is to identify phenomena in infrasound detections related to the streamers; we
100 focus on deviations of the azimuth of signal arrivals, trace velocity, signal amplitude, and
101 frequency. Dedicated studies demonstrated that from the observed signal trace velocity,
102 information about the signal refraction height can be derived (Lonzaga, 2015). If the source of
103 received signals is well defined in time and space, mean atmospheric cross-winds along the
104 signal propagation path can be estimated from back-azimuth deviations and time of signal
105 propagation (Blixt et al., 2019). Fluctuations of signal frequency and amplitude are, besides
106 variability of the signal source, influenced by atmospheric filtering (Sutherland and Bass,
107 2004).

108 Our study will focus on the possible utilization Doppler sounding and microbarographs for
109 description and analysis of GW behaviour and propagation in the stratosphere.

110 The structure of the paper is as follows: After the introduction, the description of the used
111 dataset and method can be found in the second section. Then we describe our results and in
112 the last section we discuss the possible connection to previous studies.

113

114 **2) Data and methods**

115 The selection of streamer events is based on a visual inspection of global maps of total
116 ozone column (TCO), accessible through a service provided by DLR
117 (<https://atmos.eoc.dlr.de/>) measured by the Tropospheric Monitoring Instrument (TROPOMI)
118 aboard the Sentinel 5 Precursor (S5P) mission (see Veefkind et al., 2012 for details about
119 TROPOMI/S5P). In cases where TROPOMI/S5P data is unavailable, measurements from the
120 Global Ozone Monitoring Experiment-2 (GOME-2) on the Metop series of satellites are
121 utilized. Both instruments operate in a nadir-viewing configuration on near-polar sun-
122 synchronous orbits. Further specifics regarding TCO measurements by TROPOMI/S5P are
123 elaborated by Spurr et al. (2022). The TCO retrieval process is built upon the predecessor
124 instrument's processor (GOME-2 on Metop-AB, see Munro et al. (2006) and Munro et al.

125 (2016)). For detailed information on the GOME-2 retrieval algorithm, refer to Loyola et al.
126 (2011).

127 In this paper, a streamer is identified the ozone column concentration of the finger-like
128 structure above the Northern Atlantic/Western Europe is lower than 300 DU and persists for
129 at least 3 days. The longitudinal extension is of approx. 15 to 30 degrees in the mid-latitudes
130 (between 30 to 70°N). The northernmost point of a streamer northernmost 50°N. Fig. 1 shows
131 a streamer event above the Northern Atlantic, indicated by the blue color which represent the
132 low ozone concentrations. The streamer shown in Fig. 1 is considered as an example of a
133 large event since it extends to latitudes beyond 70°N. At the western and eastern flanks of the
134 streamer, the ozone concentration exceeds 350 DU, defining distinct boundaries. As seen in
135 Fig. 1 from the green colors at the eastern coast of Northern America and western Europe.
136 The gradient of the ozone concentration in this case is about 50 DU / 5°. Furthermore, the
137 streamer is associated with a discernible pattern of circulation, with air masses being
138 meridionally deflected, which contributes to its formation and maintenance. These air masses,
139 characterized by their movement from south to north at the eastern flank and from north to
140 south at the western flank, play a significant role in the streamer's dynamics. This is the
141 reason why equatorial low ozone concentration is transported northward. In contrast, calm
142 periods, which represent the opposite dynamic situation to streamer events, are characterized
143 by very few meridionally deflected air masses. During these periods, the ozone concentration
144 in the mid-latitudes above the Northern Atlantic is consistently higher than 350 DU,
145 indicating stable atmospheric conditions and minimal perturbations in the ozone distribution.
146 An example for a calm period is shown in Fig. 2.

147 The streamer events are selected by eye for this study (results see Table 1) using the TO3
148 global maps from January 2020 and March 2021. As planetary waves are permanently
149 disturbing the atmospheric dynamic of the higher troposphere / lower stratosphere, especially
150 smaller scale streamers in particular can be observed almost every day and the identification
151 of streamer events becomes subjective. We therefore focus on a few events which are
152 comparatively strong in their evolution from our perspective. Moreover, we focus on streamer
153 events above the Northern Atlantic. Whenever additional streamer events occur somewhere
154 other than over the Northern Atlantic region with comparable spatiotemporal extent, we
155 eliminate this date from consideration as a streamer event. We assume that the effects of the
156 streamers superimpose and a distinct backtracking to the streamer over the Northern Atlantic
157 is possible. This means, that the analysis of the streamer events can be blurred to some extent.

158 We consider dates from January 2020 to April 2021. In general, planetary waves drive the
 159 Brewer Dobson Circulation in the stratosphere during winter and ozone-poor air masses are
 160 transported northward. Northern hemisphere streamer events are therefore detected between
 161 September and March. The streamer events are distinguished if they have a large spatial size,
 162 high intensity (low TO3 concentration) and if air masses are irreversibly mixed into the
 163 surrounding atmosphere. All the selected events persist for several days, but no longer than 10
 164 days.

165 To evaluate whether streamer events effect the smaller-scale atmospheric dynamics, calm
 166 events are also identified through subjective criteria. These events serve as a background
 167 reference for streamer events, since large-scale spatial structures are absent in their TO3. The
 168 events are selected when the meridional gradient of ozone concentration from the equator to
 169 the polar region on the Northern Hemisphere exhibit minimal longitudinal variation.
 170 Examples of calm atmospheric dynamics are listed in Table 1 (right).

171

Streamer events		Calm periods	
From	To	From	To
06.02.2020	10.02.2020	02.03.2020	08.03.2020
11.2.2020	13.2.2020	09.03.2020	14.03.2020
31.08.2020	03.09.2020	28.03.2020	10.04.2020
05.09.2020	11.09.2020	19.04.2020	27.05.2020
03.11.2020	07.11.2020	9.11.2020	15.11.2020
21.11.2020	25.11.2020	12.12.2020	22.12.2020
23.02.2021	27.02.2021	30.12.2020	06.01.2021
09.03.2021	12.03.2021	21.01.2021	20.02.2021
		28.02.2021	07.03.2021
		13.03.2021	24.03.2021

		29.03.2021	07.04.2021

172 **Table 1** Streamer events above Northern Atlantic from January 2020 until March 2021 and
173 related start and end dates(two left columns). Calm periods are listed in the two column on the
174 right.

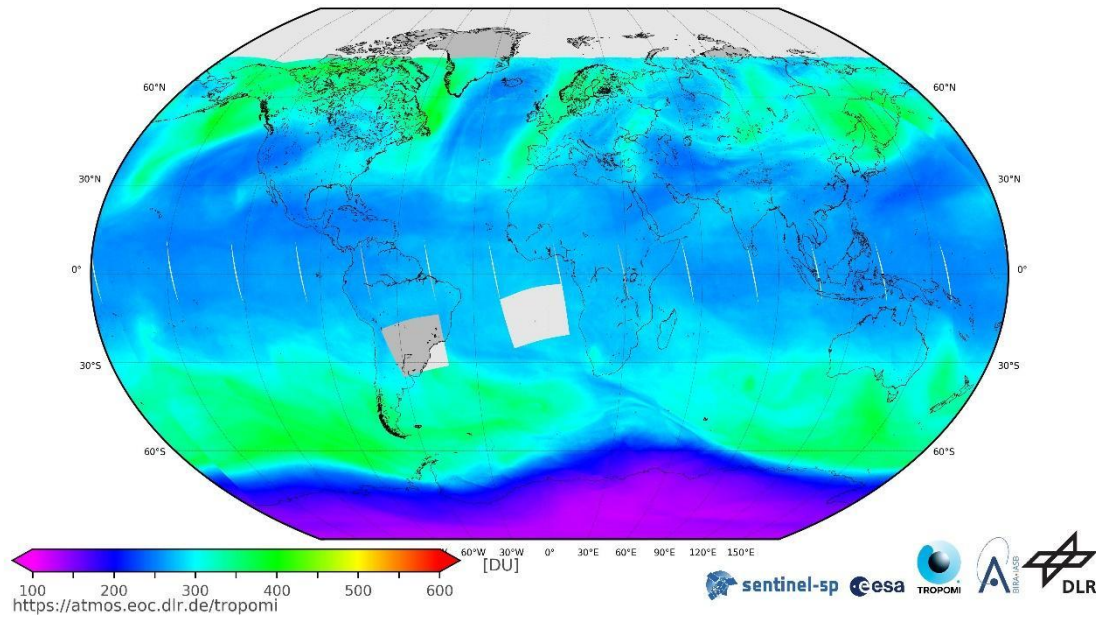
175

176 Figure 1 shows the TCO from TOPOMI/S5P integrated from November 3rd to November 5th
177 2020. Ozone-poor air masses (blue) are located above the Northern Atlantic from 30°N to
178 70°N along with smaller scale ozone-poor air masses above western North America and
179 Central Asia. The TO3 concentration is disturbed by planetary waves around latitude circles,
180 which lead to wave structures visible especially at the transition of blue to green colors. A
181 large streamer event of ozone-poor air masses is detected over the Northern Atlantic. A small
182 streamer can be detected over western North America. There are also ozone-poor air masses
183 above eastern Europe. The temporal evolution shows, that the ozone-poor air masses above
184 eastern Europe are due to a decaying streamer which evolved several days earlier. As
185 planetary waves are more or less permanently disturbing the atmospheric dynamics,
186 especially smaller scale streamers can be detected almost every day. In this example, the
187 streamer event above the Northern Atlantic is largest. Therefore, we consider this event for
188 the further analysis.

O₃

Ozone total column

Acquisition Time	Plot Range	Sensor	Algorithm
03-November-2020 23:03:33 05-November-2020 00:39:28	Min: 79.46237 - Max: 490.4168	TROPOMI S5P	UPAS-O3-DOAS_CAL-5.1.0 UPAS2 02.01.03



189

190 Fig. 1. TCO by TROPOMI/S5P from November 3rd to November 5th 2020 shows ozone poor
191 airmasses above the Northern Atlantic as an example of a streamer event for the further
192 analysis. Colors (from violet to red) indicate the total ozone column concentrations (from low
193 to high) in Dobson Units. Source: DLR, CC-BY 3.0

194

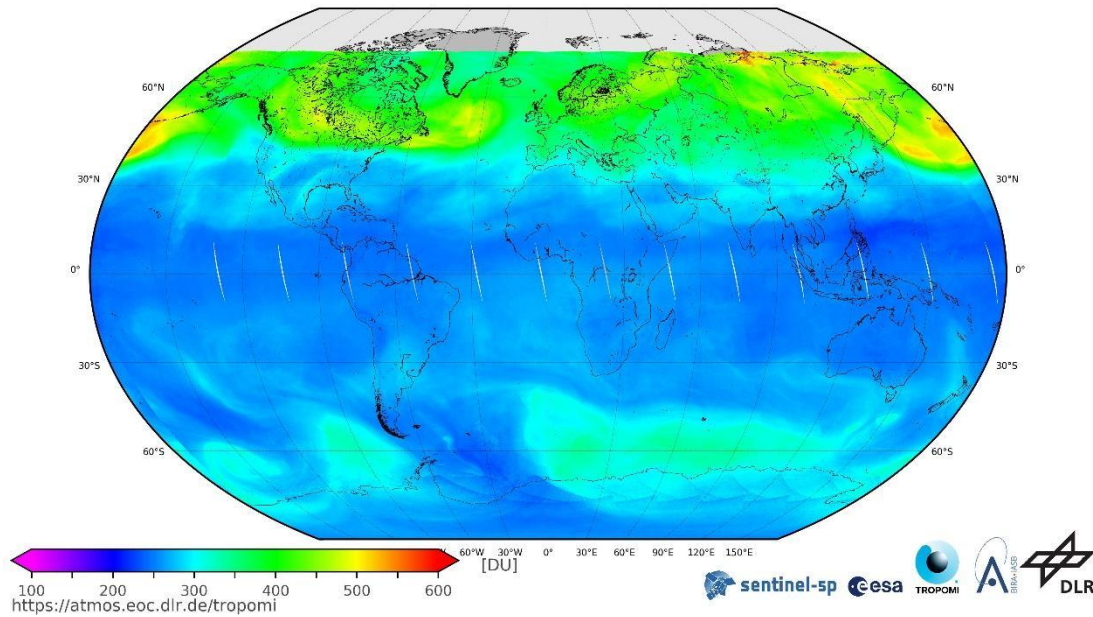
195 Figure 2 shows the TCO from TOPOMI/S5P from February 11th to February 13th 2020. The
196 event is characterized by a strong meridional gradient from the equatorial to polar region on
197 the Northern Hemisphere with almost no longitudinal variation. Therefore, we consider this
198 event as an example of the calm period for further analysis.

199

O₃

Ozone total column

Acquisition Time	Plot Range	Sensor	Algorithm
11-February-2021 23:02:25 13-February-2021 00:57:37	Min: 194.2067 - Max: 701.0549	TROPOMI S5P	UPAS-O3-DOAS_CAL-5.1.0 UPAS2 02.01.04



200

201 Fig. 2. TCO by TROPOMI/S5P from February 11th to February 13th 2020 as an example of
202 calm atmospheric dynamics. A clear meridional gradient of ozone can be observed on the
203 Northern Hemisphere without large-scale wave structures. Colors (from violet to red) indicate
204 the total ozone column concentrations (from low to high) in Dobson Units. Source: DLR, CC-
205 BY 3.0

206 Two stations from the Czech microbarograph network (Bondar et al., 2022) are involved in
207 the study – the large aperture array WBCI (50.25°N 12.44°E) and the small aperture array
208 PVICI (50.52°N 14.57°E). To study the propagation of GW and long-period infrasound (from
209 acoustic cut-off up to about 2.5 s) pressure recordings at WBCI are utilized. Four sensors of
210 the WBCI array are arranged in a tetragon. The inter-element distances of 4 – 10 km provide
211 optimum performance in the infrasound frequency range from the acoustic cut-off frequency
212 of 0.0033 to 0.0068 Hz (Garcès, 2013). The WBCI array with its large inter-element distances
213 has a unique configuration compared to the arrays of the International Monitoring System of
214 the Comprehensive Nuclear Test Ban Treaty Organisation which are for infrasound
215 monitoring in the frequency band of 0.02 – 4 Hz (Marty, 2019). Each array element at WBCI
216 is equipped with an absolute microbarometer of the type Paroscientific 6000-16B-IS with
217 parts-per-billion resolution. A GPS receiver is used for time stamping. Data are stored with a
218 sampling rate of 50 Hz. For infrasound monitoring, WBCI data are resampled at sampling rate
219 of 10 Hz. To detect and analyze GWs, 1-min mean values of the absolute pressure data are
220 used.

221 The small aperture array PPCI provides optimal detection precision in the frequency range of
 222 0.14 – 3.4 Hz (Garcès, 2013). Three sensors are arranged in an equilateral triangle; the array
 223 aperture is 200 m. The differential sensors of the type Infrasound Gage ISGM03
 224 manufactured by the Scientific and Technical Centre, give a flat response in the frequency
 225 range of 0.02 – 4 Hz. A GPS receiver is used for time stamping. The data are stored with a
 226 sampling frequency of 25 Hz. This sampling rate is also used in regular processing of
 227 infrasound detections at PPCI.

228 Infrasound detections are processed using the DTK-GPMCC software, the core of which is
 229 the Progressive Multi-Channel Correlation (PMCC) detection algorithm (Cansi, 1995; Le
 230 Pichon and Cansi, 2003). PMCC analyses pressure recordings from an infrasound array and
 231 looks for coherent signals in overlapping time windows in several frequency bands (Le
 232 Pichon and Cansi, 2003). An elementary detection with the PMCC, or the detection pixel is
 233 declared in the time-frequency window, when signal correlation and consistency criteria are
 234 met. Detection pixels are grouped into the detection families based on similar time, frequency,
 235 azimuth of signal arrival, and signal trace velocity (Brachet et al., 2010). The arrival
 236 parameters of the detected infrasound are stored in the detection bulletins. The parameters of
 237 interest for the present study include time of arrival, azimuth of arrival, trace velocity,
 238 frequency, and amplitude. The PMCC configuration is set on an individual basis and is
 239 optimized for the given array (Brachet et al., 2010; Garcès, 2013; Szuberla et al., 2004); the
 240 main parameters of the DTK-GPMCC settings for the arrays PPCI and WPCI are given in
 241 Table 2.

Station	PPCI	WPCI
Detection range	0.09-7 Hz	0.0033-0.4 Hz
Number of detection bands	19	11
Length of the detection window; frequency dependent	412.84-6.44 s	2555-118 s
Adjacent windows overlap	95 %	90 %
Consistency	0.1 s	3 s
Azimuth tolerance for families forming	10°	3°
Family size	10-50 pixels	15-50 pixels

Frequency range analysed in the study of streamer events	0.09-0.4 Hz	0.0033-0.4 Hz
--	-------------	---------------

242

243 **Table 2.** Main parameters of the DTK-GPMCC configurations for the arrays PPCI and
 244 WBCI.

245

246 InfraGA/GeoAc raytracing tools are employed to study infrasound ducting in the atmosphere
 247 (Blom and Waxler, 2012; Blom, 2019). Infrasound raytracing provides an easy-to-interpret
 248 approximation of infrasound propagation and can help to identify possible modifications of
 249 atmospheric waveguides above Eastern Atlantic and Western Europe during streamer events.
 250 It can also show whether the streamer event influences reach Central Europe. The raytracing
 251 is employed in our study for the purpose of identifying azimuths and distances from the
 252 source that can be influenced by the streamer event. Hence, it can reveal whether these
 253 influences reach Central Europe directly or whether the signals are ducted to the region
 254 through the waveguide in the upper stratosphere or thermosphere as occurs in quiet periods.
 255 InfraGA/GeoAc provides simulations of signal propagation from a point source; propagation
 256 through the range dependent atmosphere is modelled in the present study. Atmospheric
 257 characteristics are obtained from the G2S model (Drob et al. 2003). Vertical profiles of
 258 temperature, zonal and meridional winds, density and pressure are an input for the
 259 InfraGA/GeoAc. The grid of profiles covers the area from 45° to 65°N and from 30°W to
 260 22.5°E; the latitudinal step is 5° and longitudinal step is 7.5°.

261 Propagation of GWs in the thermosphere/ionosphere is studied using the multi-point and
 262 multi-frequency continuous Doppler sounding system located in Czechia. Its advantage is a
 263 high time resolution (around 10 s) relative to ionospheric sounders (ionosondes) that measure
 264 the profile of electron densities in the ionosphere. Observed frequency shifts are due to the
 265 motion and electron density changes in the ionospheric plasma, caused for example by
 266 interaction with atmospheric waves propagating in the neutral atmosphere, with which the
 267 ionosphere (above ~ 80 km) merges. The sounding radio signal is reflected at the height,
 268 where its frequency matches the so called local plasma frequency, which is determined by the
 269 local electron density. Therefore, the reflection height changes during the day and depends on
 270 the sounding frequency. Significant Doppler shifts, usable for analysis, are obtained if the
 271 signal is reflected from the so called ionospheric F2 layer (approximately 200 – 300 km).
 272 Several sounding frequencies are used in Czechia. The 3.59 MHz sounding was mostly

273 effective at night, while the 4.65 MHz sounding provided good daytime data during the period
274 analyzed. The propagation characteristics of GWs are calculated from the time delays
275 between signals observed at the respective sounding paths (reflection points for each
276 transmitter-receiver pairs) assuming that the reflection points are at the midpoints between
277 each transmitter and receiver. A 60 or 90 min long time interval is usually used to calculate
278 the velocities and azimuth of the observed waves. The methods are described in detail by
279 Chum and Podolska (2018). The two-dimensional (2-D) version (propagation analysis in a
280 horizontal plane only) is anticipated for most of the studies, since a 3-D analysis requires
281 simultaneous observation and signal correlation at different frequencies, which is often not the
282 case, especially during solar minimum. Results of statistical investigation have been recently
283 published (Chum et al., 2021). Identical methods of propagation analysis have been applied
284 to investigate propagation of GWs in the troposphere based on data from the large-aperture
285 array WBCI (here the time delays are related to the locations of individual microbarometers).
286 All analyses will be done with respect to the streamer events and calm periods shown in Table
287 1.

288 **3) Results**

289 **3.1 Infrasound observations at ground microbarograph arrays WBCI and PPCI in** 290 **November 2020 and in March 2021**

291 Wave activity in the infrasound frequency range of 0.0033-0.4 Hz is investigated combining
292 observations at the stations WBCI and PPCI. Infrasound detections at WBCI are processed in
293 the frequency band of 0.0033 – 0.4 Hz. The operational range of the array is extended above
294 the upper limit of the optimum array range; the degraded performance of WBCI at
295 frequencies higher than 0.0068 Hz shall be considered. The upper limit of the analysed band
296 is intentionally set to 0.4 Hz to cover microbaroms. PPCI detections are analysed in the
297 frequency range of 0.09 – 0.4 Hz. The band partly overlaps with the detection range of the
298 WBCI array and at frequencies of 0.12 – 0.35 Hz it is dominated by microbaroms (e.g.,
299 Campus and Christie, 2010). Unlike WBCI, PPCI provides an optimal performance in the
300 microbarom band.

301 Microbaroms are infrasound signals generated by a non-linear interaction of ocean waves
302 travelling in opposite directions. Microbaroms form a wide peak around 0.2 Hz in the
303 infrasound spectrum; their frequency corresponds to twice the frequency of sea waves. A
304 powerful source of microbaroms is located in the North Atlantic and the signals are regularly

305 detected by European stations (Hupe et al., 2019). The detection capability of microbaroms
306 from the North Atlantic is particularly high from October to March when the source becomes
307 stronger due to stormy weather above the ocean and signal propagation to the East from the
308 source is supported by the stratospheric waveguide (Landès et al., 2012). From the global
309 point of view, microbaroms are permanently present in recordings of infrasound stations
310 worldwide.

311 Streamer events often occur above the North Atlantic. Thus, microbaroms propagating from
312 the North Atlantic to the continental Europe can travel through the region influenced by a
313 streamer event and the detections at infrasound stations in Europe can show signatures of
314 streamer events.

315 We analyse infrasound observations from 3rd to 25th November 2020 and from 28th
316 February to 25th March 2021 with focus on microbaroms. In these time intervals adjacent
317 streamers and calm periods occurred (Table 1). Streamer events and the calm period in the
318 November 2020 time window are evaluated separately from those in the March 2021 time
319 window to avoid seasonal influences. While a well-developed eastward stratospheric
320 waveguide can be expected in November, its efficiency can decrease in March due to the
321 seasonal reversal of stratospheric winds.

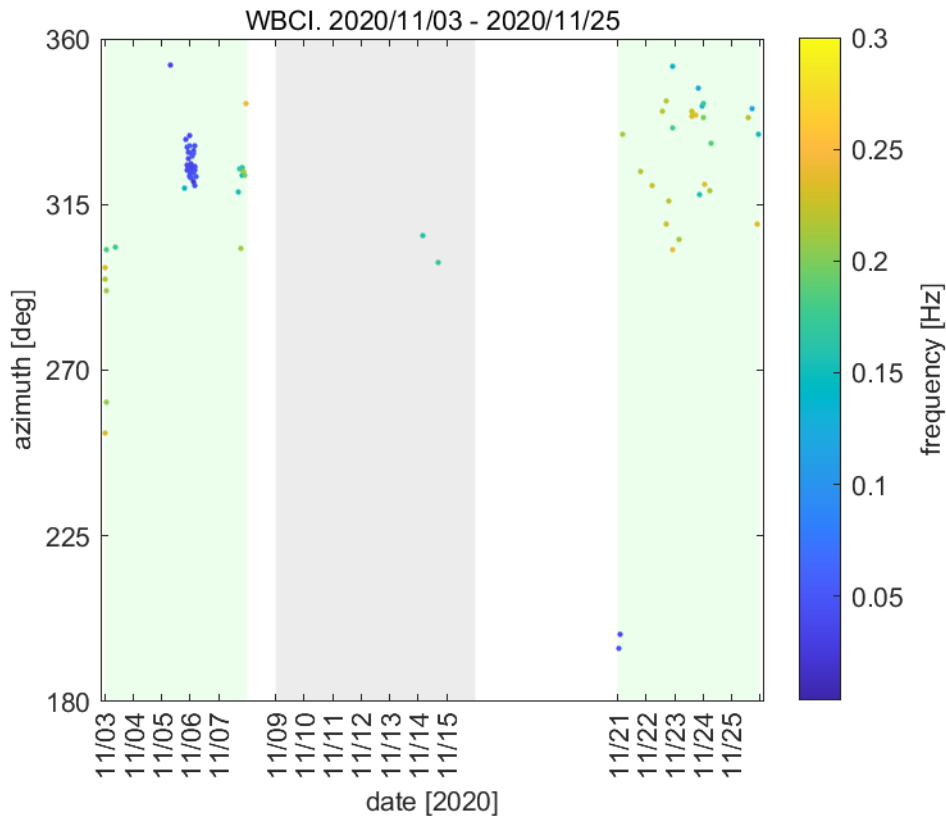
322

323 **3.1.1 Infrasound observations from 3rd to 25th November 2020**

324 Two streamer events developed in November 2020. The first streamer occurred from 3rd
325 to 7th November and the second one from 21st to 25th November. The streamers were
326 separated by a calm period from 9th to 15th November.

327 The most important phenomena found in the infrasound arrival parameters are fluctuating
328 signal frequency and fluctuating signal amplitude.

329 WBCI provides rather sparse detections during both streamer events and only two
330 detection families are obtained during the seven-day calm period (Figure 3). The
331 frequencies near 0.2 Hz and back-azimuths of 290° – 350° indicate that the observed
332 signals are likely microbaroms from the North Atlantic. A decrease of the signal frequency
333 is observed during the first streamer event. On 5th – 6th November from 20 to 05 UTC, the
334 mean frequency of the north-west arrivals drops down to 0.04 Hz, below the microbarom
335 frequency range. During the second streamer event from 21st to 25th November, the signal
336 frequency is stable around 0.22 Hz. An increase of the amplitude from the mean value of
337 0.019 Pa to 0.035 Pa is observed from 23rd November, 18 UTC until the end of the analysed
338 time period on 25th November at 24 UTC.



340

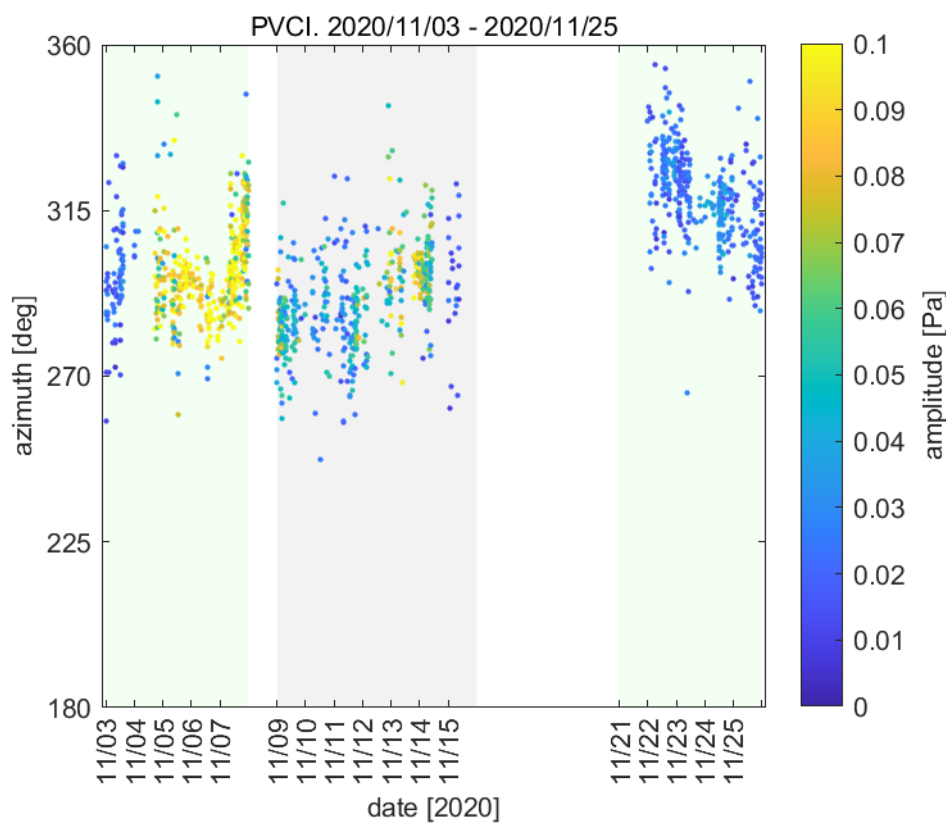
341 Fig. 3. Infrasound observations at WBCI on 3rd - 25th November 2020. Azimuth of signal
 342 arrivals is shown; the colorbar refers to the mean frequency of the detection family. One circle
 343 in the plot represents one detection family. Green background marks the streamer events, grey
 344 background marks the calm period.

345

346 Similar to the back-azimuths at WBCI, PNCI detects arrivals from the north-west in the
 347 analysed frequency range of 0.09 – 0.4 Hz (Figure 4). Fluctuating signal amplitudes are
 348 observed. Values around 0.020 Pa occur on 3rd November. From 4th November, 18 UTC to 7th
 349 November, 22:30 UTC, the signals are of amplitudes around 0.089 Pa. The amplitudes
 350 decrease to the values around 0.046 Pa during the following quiet period on 9th – 15th
 351 November. Microbarom amplitudes fluctuate between 0.013 and 0.036 Pa (1st decile and 9th
 352 decile, respectively) during the streamer event on 21st – 25th November. Publicly available
 353 data such as meteorological charts provided by Deutscher Wetterdienst and the
 354 WAVEWATCHIII® wave-action model (The WAVEWATCHIII® Development Group,
 355 2016) indicate that there are maritime storms in the North Atlantic within the analysed time
 356 window from 3rd to 25th November 2020. Maximum heights of sea waves are predicted in the
 357 North Atlantic near south coast of Greenland and Island from 5th to 6th November, from 12th

358 to 13th November, and on 20th November. The height of combined wind waves and swell
 359 reaches 10 m. As mentioned in section 3.1 it is not only the wave height but also the wave
 360 direction (waves propagating in opposite directions) that determines the microbarom source.
 361 Nevertheless, fluctuating intensity of the microbarom source shall be taken into account
 362 during maritime storms. As a consequence, fluctuating microbarom amplitudes can be
 363 observed at the infrasound stations.

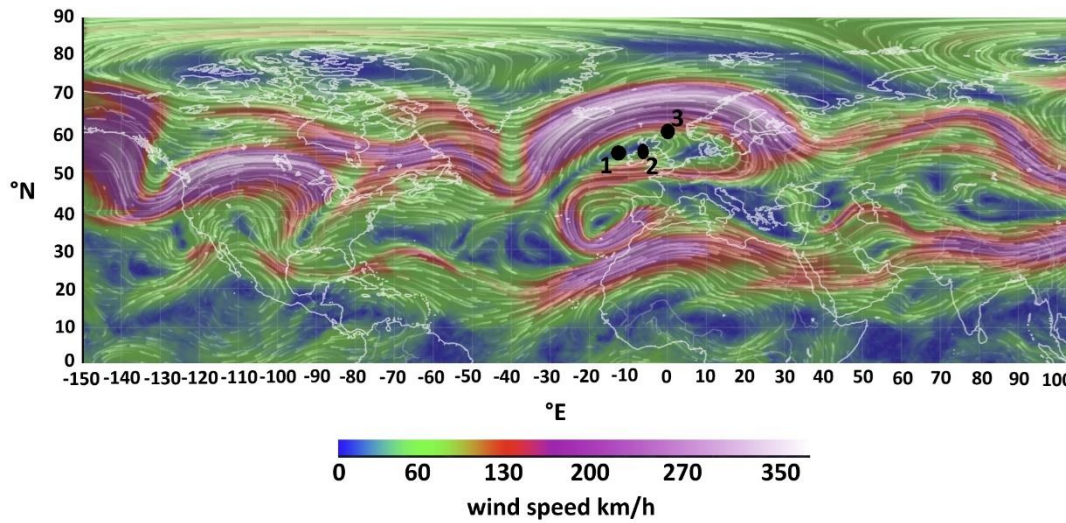
364
 365
 366



367
 368 Fig.4. Infrasound observations at PVC I on 3rd - 25th November 2020. Azimuth of signal
 369 arrival is shown; the colorbar refers to the signal amplitude. Green background marks the
 370 streamer events, grey background marks the calm period.

371
 372 To study propagation of signals from sources located at the surface of the North Atlantic
 373 the InfraGA/GeoAc tools are employed. The fictitious point sources are located (1) at 55°N
 374 and 15°W, (2) at 55°N and 5°W, and (3) at 60°N and 0°longitude. The coordinates of the
 375 sources are estimated based on the position of the tropopause jet stream disturbance. Point
 376 (1) is located under the northward jet-stream, point (3) under the southward jet-stream, and

377 point (2) is located between those two opposing branches of the jet stream disturbance, see
378 Figure 5.



379
380

381 Fig.5. Wind field at the pressure level of 250 hPa on 06 November 2020 at 00 UTC. A
382 disturbance of the jet-stream above the eastern North Atlantic and the British Isles is caused
383 by the streamer event. Figure taken from earth.nullschool.net

384

385 A multi azimuth simulation is run on 6th November at 00 UTC. The simulation is performed
386 at the time point in the middle of the streamer event when a maximum stage of the
387 phenomenon can be expected. Taking into account the mutual locations of the sources and the
388 receiving arrays, eastward signal propagation is modelled. The azimuth limits are set to 0° and
389 180°, the azimuth step is 3°. Rays are launched with inclinations of 2° - 45°; the step is 2°.
390 Information is obtained through which waveguides the signal can possibly arrive to the
391 infrasound stations and their surroundings. The reason why arrivals **to extended areas around**
392 **the stations** are considered is that signal propagation from three fictitious point sources stands
393 in for a real source, the surface of the North Atlantic where microbaroms are generated.
394 Therefore, the model outputs must be taken as an approximation of the real situation. The
395 turning height and ground reflections of the 0.2 Hz signal are obtained in the multi azimuth
396 simulation. The results are visualised in Figure 6 and in supplementary materials. The red
397 asterisk represents the point source. The concentric sectors of circles show i.e. regions of
398 ensonification, regions where the signal emitted by the source can be recorded at an
399 infrasound station. The dots showing signal ground reflections are organized in a radial
400 pattern. Each of the lines of this pattern represents one azimuth of signal propagation for

401 which the multi azimuth simulation is run; the azimuth step is 3° . The colours of the dots
402 inform about the turning height of the ray and thus provide information about signal ducting
403 in the waveguides. Depending on the turning height, infrasound is subject to attenuation of
404 variable strength when it propagates through the atmosphere. Infrasound attenuation is low in
405 the stratospheric waveguide. Strong absorption occurs in the thermospheric waveguide; the
406 absorption is higher at higher signal frequencies (Sutherland and Bass, 2004). To obtain the
407 view of signal attenuation along the raypath in the vertical plain a single azimuth simulation
408 is employed. The single azimuth simulation is run along the azimuths from the fictitious
409 sources (1) – (3) to the stations WBCI and PPCI; it is obtained for the frequencies of 0.04 Hz
410 and 0.2 Hz. As a reference, a multi azimuth propagation of the 0.2 Hz signal is modelled from
411 a source at 55°N and 15°W on the calm day 12th November at 00 UTC. The time point in the
412 middle of the calm period between two streamer events is selected to minimize possible
413 effects of the subsiding and arising streamer event, respectively.

414 First, we focus on infrasound propagation from the North Atlantic to Central Europe. Signal
415 arrivals only through the thermospheric waveguide are enabled from the source at 60°N and
416 0° longitudes (Figure 6) during the streamer event on 6th November 2020 at 00 UTC.

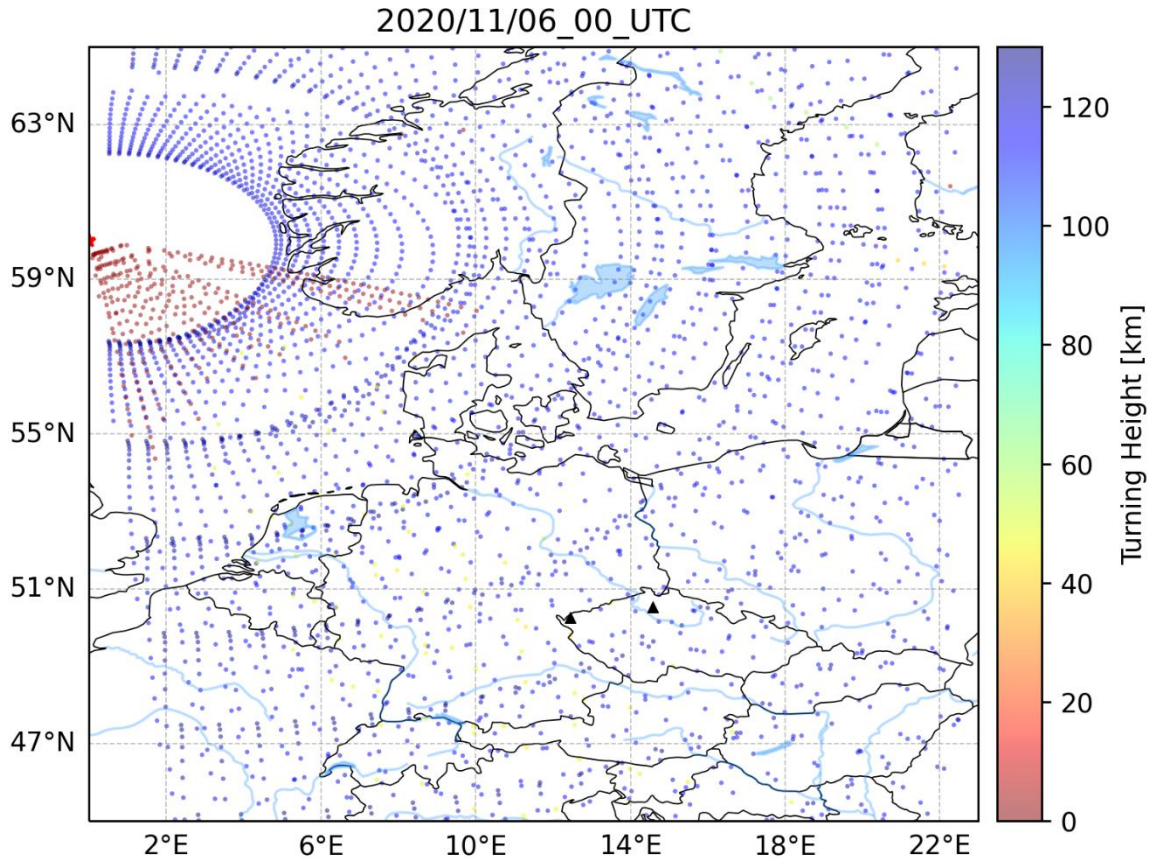
417 Stratospheric and thermospheric ducting are possible from the sources at 55°N 15°W and
418 55°N 5°W to Central Europe (supplementary materials). Similarly, stratospheric and
419 thermospheric ducting is predicted from the source at 55°N 15°W to Central Europe on the
420 calm day 12th November 2020 (supplementary materials). Signal propagation only through the
421 thermospheric waveguide is enabled from the source at 60°N and 0° longitude (Figure 6). The
422 distances between the fictitious sources and the stations are 1300 – 2000 km. The amplitude
423 loss of the 0.2 Hz signal in the thermospheric waveguide at these distances is 100 dB relative
424 to the amplitude at a distance of 1 km from the source. According to the simulations,
425 observations of the thermospheric arrivals of microbaroms are unlikely at PPCI and WBCI
426 due to strong signal attenuation. Microbaroms apparently arrive to Central Europe through the
427 stratospheric waveguide formed in the upper stratosphere during the streamer events as well
428 as on the calm day. Indeed, arrivals from the back-azimuths of 285° - 315° are dominant at
429 PPCI from 3rd to 7th November. Those back-azimuths correspond to the positions of the
430 fictitious sources at 55°N 15°W and at 55°N 5°W , while the back-azimuth to the source at
431 60°N and 0° latitude is 325° . The amplitude loss of the 0.04 Hz signal at the distances of 1300
432 – 2000 km from the source is 60 – 80 dB. In general, thermospheric arrivals of this low
433 frequency signal are not strictly rejected. However, in our case the 0.04 Hz signal arrives with

434 trace velocity around 0.330 km/s at WBCI. The low trace velocity indicates signal
435 propagation in the troposphere/lower stratosphere waveguide (Lonzaga, 2015).

436 Next, we study the influences of the streamer event related disturbance anywhere in the
437 modelled region. The disturbance of the jet stream can modify signal propagation up to
438 distances of several hundreds to a thousand km from the source; the influenced azimuth
439 range is limited. Signals from the source at 55°N and 15°W can propagate in the tropopause
440 waveguide in azimuths between 10° and 60° up to the distance of ~1000 km. The amplitude
441 loss of the 0.2 Hz signal at a distance of 1000 km is 60-70 dB relative to the amplitude at 1
442 km from the source. The southward branch of the jet-stream disturbance enables infrasound
443 propagation in the tropospheric waveguide in azimuths of 100 - 160° from the source at
444 60°N 0° longitude. Maximum distance which the signal can travel in the south-east direction
445 is ~600 km. The amplitude loss of the 0.2 Hz signal at a distance of 600 km is 60 dB
446 relative to the amplitude at 1 km from the source.

447 The observations and the model outputs during the November 2020 event can be
448 summarized as follows: infrasound arrives from sources in the North Atlantic to Central
449 Europe mainly through the stratospheric waveguide formed between the ground and upper
450 stratosphere. The jet-stream disturbance above the eastern North Atlantic does not have an
451 impact on infrasound arrivals in Central Europe on 6th November 2020 at 00 UTC.
452 Fluctuating signal amplitudes are likely a consequence of fluctuating intensity of the
453 microbarom source during maritime storms. The decrease of signal frequency at WBCI is
454 not caused by a transient change in signal ducting and by the related signal filtering in the
455 thermospheric waveguide.

456



457
 458 Fig.6. Modelled infrasound propagation from a point source located at 60°N and 0°longitude
 459 (red asterisk) during the streamer event on 6th November 2020 at 00 UTC. The colorbar
 460 refers to the turning height (maximum height) of the signal. Red color indicates signal
 461 propagation in the waveguide formed near the tropopause (altitudes around 10 km), arrivals
 462 through the thermospheric waveguide are shown in blue (altitudes above 100 km). Black
 463 triangles represent infrasound arrays WBCI (the left triangle) and PVICI (the right triangle).
 464

465 **3.1.2 Infrasound observations from 28th February to 24th March 2021**

466 Another streamer event occurred from 9th to 12th March 2021 preceded and followed by
 467 calm periods from 28th February to 7th March and from 13th to 24th March, respectively.

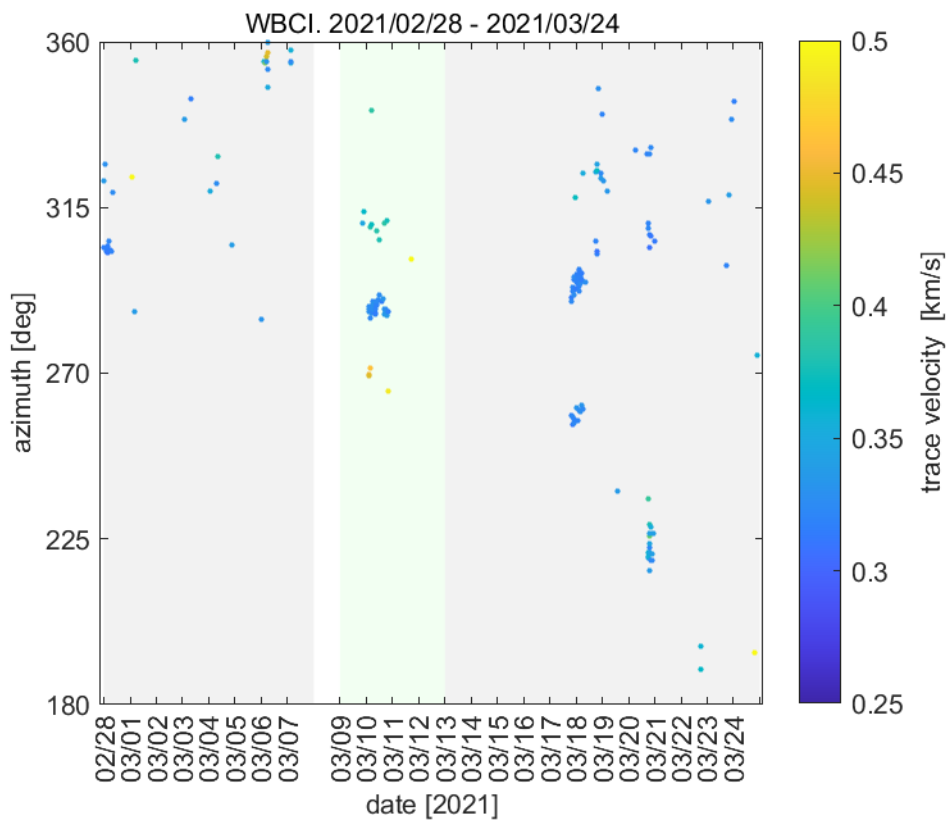
468 The most important phenomenon identified in the infrasound arrival parameters is a
 469 fluctuating trace velocity.

470 Both WBCI and PVICI detect signals arriving from the north-west, from back-azimuths of
 471 285° – 310°. An increase of signal trace velocities is observed in some of the detections at
 472 WBCI during the streamer event compared to calm periods (Figure 7). On 10th March at 00 –
 473 06 UTC, trace velocities of 0.460 km/s and 0.380 km/s are observed from back-azimuths of
 474 270° and 310° respectively. It is by 0.05 – 0.13 km/s higher than on the calm days. On the

475 other hand, signals from the back-azimuth of 288° arrive with the trace velocity of 0.330 km/s
 476 within the same time window, this velocity corresponds to that on the calm days. Effects of
 477 spatial aliasing shall be taken into account when evaluating the detections. The signal
 478 frequencies are around 0.2 Hz, well above the range of array optimum performance. The
 479 observed different trace velocities at WBCI can therefore be a processing bias rather than a
 480 consequence of variations in signal ducting.

481 In contrast to the WBCI observations, PVEC records a decrease in trace velocities on 10th
 482 March at 00 – 06 UTC (Figure 8). Trace velocities of 0.377 km/s are observed compared to
 483 0.413 km/s and 0.395 km/s during the calm periods before and after the streamer,
 484 respectively.

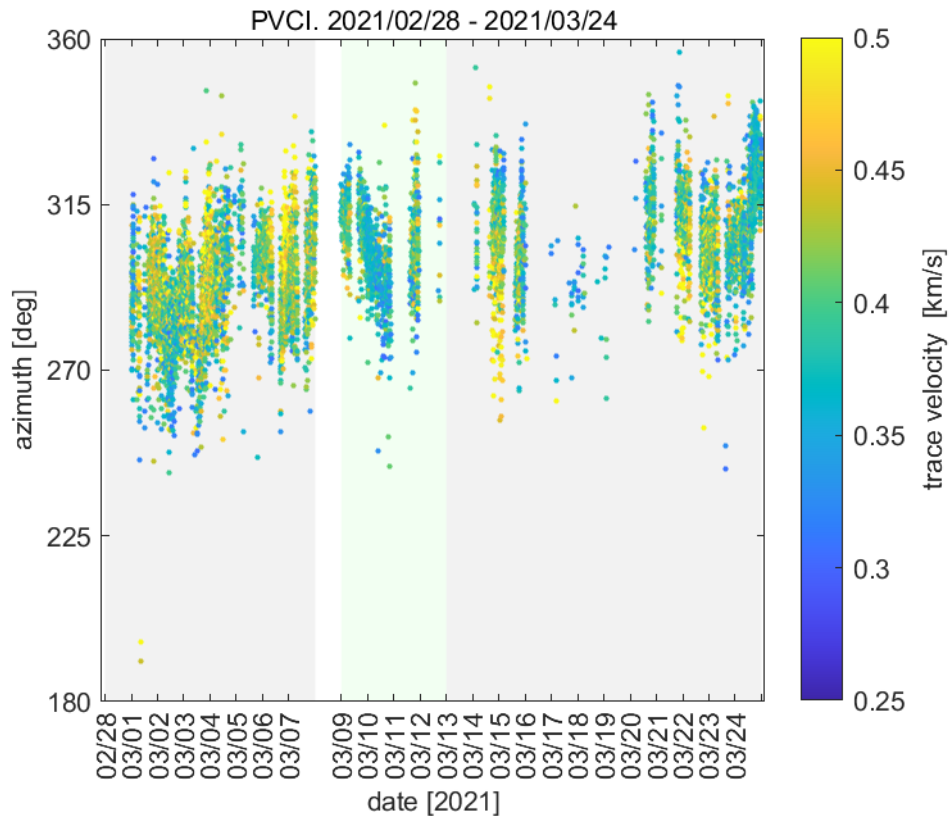
485



486

487 Fig.7. Infrasound observations at WBCI on 28th February – 24th March 2021. Azimuth of
 488 signal arrival is shown; the colorbar refers to the signal trace velocity. Green background
 489 marks the streamer event, grey background marks the calm periods.

490



491

492 Fig.8. Infrasound observations at PVC I on 28th February – 24th March 2021. Azimuth of
 493 signal arrival is shown; the colorbar refers to the signal trace velocity. Green background
 494 marks the streamer event, grey background marks the calm periods.

495

496 Changes of the trace velocity can indicate changes of the refraction altitude of the signal
 497 (Lonzaga, 2015). The exact limits of the trace velocity for the given atmospheric waveguide
 498 depend on the current state of the atmosphere. We use the thresholds determined for a
 499 model atmosphere in Lonzaga (2015) as helpful hints for our further consideration: Trace
 500 velocities below 0.340 km/s indicate signal refraction in the troposphere and lower
 501 stratosphere. Trace velocities between 0.340 and 0.380 km/s are typical for signals ducted
 502 in the waveguide between the ground and the upper stratosphere. Signals traveling in the
 503 thermospheric waveguide arrive with trace velocities larger than 0.380 km/s.

504 The high trace velocities recorded at PVC I disprove signal refraction in the lower
 505 stratosphere. Hence, it is unlikely that the signals arrive through a waveguide that can form
 506 at the tropopause – lower stratosphere by the effect of the streamer event.

507 Like in the November 2020 case, signal propagation above the eastern North Atlantic and
 508 Western and Central Europe is investigated using the InfraGA/GeoAc tools. Propagation of
 509 the 0.2 Hz signal is modelled for 10th March at 03 UTC, in the middle of the streamer

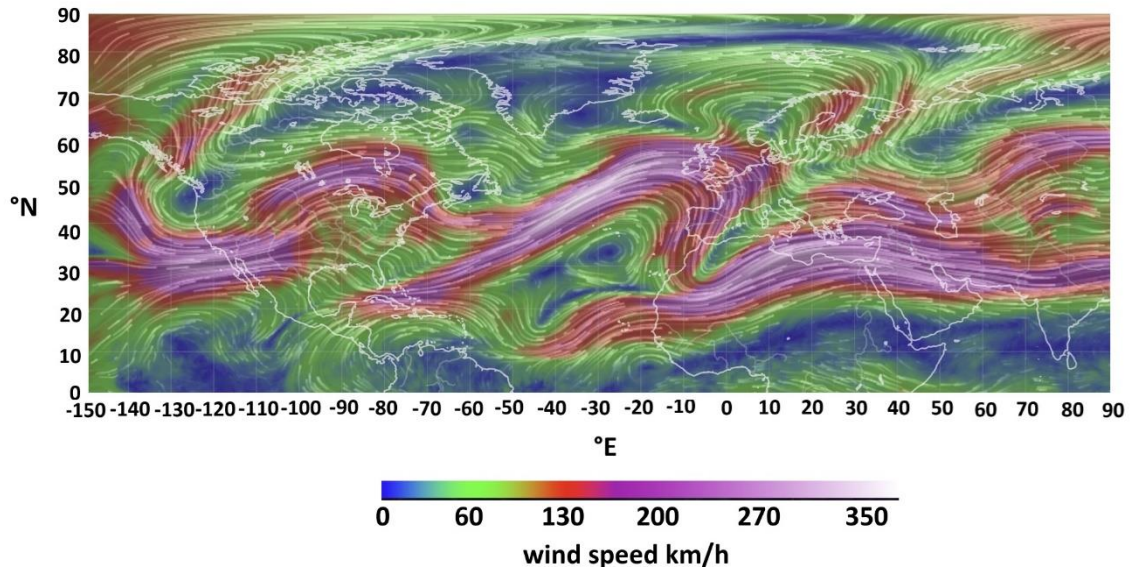
510 event. A source is located at 55°N 15°W at a distance of ~2000 km from the stations. This
511 scenario represents signal propagation from the central North Atlantic. The other source is
512 located at 55°N 0°latitude representing propagation of microbaroms from the North Sea.
513 The distance from the stations is ~1000 km. Both points are located under the jet-stream
514 disturbance related to a streamer event.

515 Eastward signal ducting is enabled in the stratospheric and thermospheric waveguides
516 from both sources to the stations. Strong signal absorption in the thermospheric waveguide
517 likely disables thermospheric arrivals to the PPCI and WBCI. We assume that signals
518 ducted in the upper stratosphere are detected. The other eastward waveguide occurs near
519 the tropopause, formed by the eastward to south-eastward jet-stream above the eastern
520 North Atlantic and Western Europe at latitudes 50 – 60°N (Figure 9). Signals from the
521 source in the North Atlantic are predicted to travel in the tropopause waveguide to distances
522 of 1000-1100 km. The signal attenuation is low in the tropopause waveguide; the relatively
523 short distance under the waveguide influence is determined by the location and extent of
524 the jet-stream disturbance. The tropopause/lower stratosphere arrivals can be detected
525 mainly on the British Isles. The waveguide does not reach to PPCI and WBCI stations (see
526 supplementary materials).

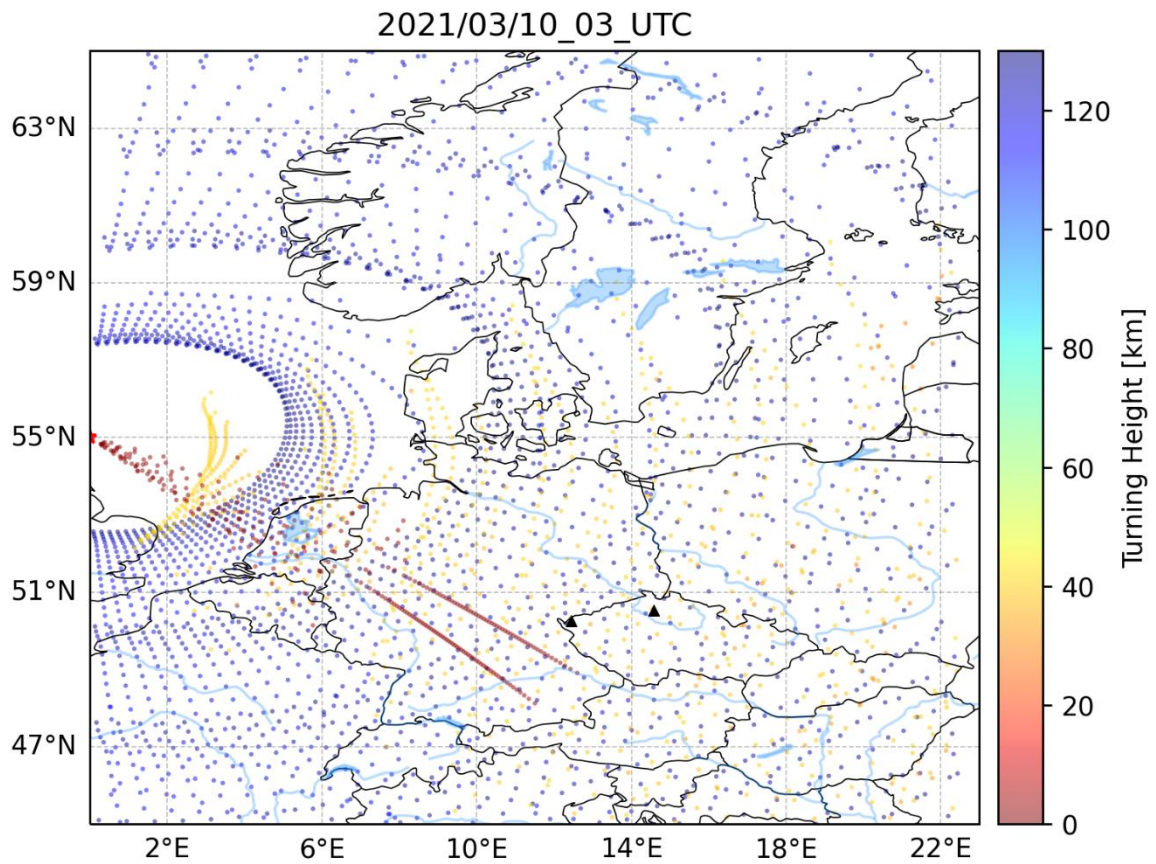
527 Signals emitted by a source in the North Sea can propagate through the tropopause
528 waveguide. The signals propagate to the south-east and are predicted to reach Central
529 Europe. The tropopause/lower stratosphere arrivals are represented by red dots in Figure
530 10. The influenced regions are to the south-west from PPCI and WBCI, several hundreds
531 of kilometers distant from the stations. The approximation of infrasound propagation
532 obtained from the raytracing is in accord with observations. The trace velocities at PPCI of
533 0.377 km/s indicate infrasound propagation in the waveguide formed between the ground
534 and the upper stratosphere rather than in the waveguide near the tropopause.

535 Like in the November 2020 case, infrasound arrivals from the North Atlantic to the
536 stations PPCI and WBCI in Central Europe are not influenced by the waveguide at the
537 tropopause – lower stratosphere. Observed trace velocities fluctuate within or close above
538 the limits that indicate infrasound propagation in the upper stratosphere during the streamer
539 event and both adjacent quiet periods.

540



541
 542 Fig.9. Wind field at the pressure level of 250 hPa on 10 March 2021 at 03 UTC. A
 543 disturbance of the jet-stream above the eastern North Atlantic and the British Isles is caused
 544 by the streamer event. Figure taken from earth.nullschool.net
 545



546
 547 Fig.10 Modelled infrasound propagation from a point source located at 55°N and 0° longitude
 548 (red asterisk) on 10th March 2021 at 03 UTC. The colorbar refers to the turning height

549 (maximum height) of the signal. Red color indicates signal propagation in the waveguide
550 formed near the tropopause (altitudes around 10 km), arrivals through the stratospheric
551 waveguide are shown in yellow (altitudes around 40-50 km) and arrivals through the
552 thermospheric waveguide are shown in blue (altitudes above 100 km). Black triangles
553 represent infrasound arrays WBCI (the left triangle) and PPCI (the right triangle).

554

555

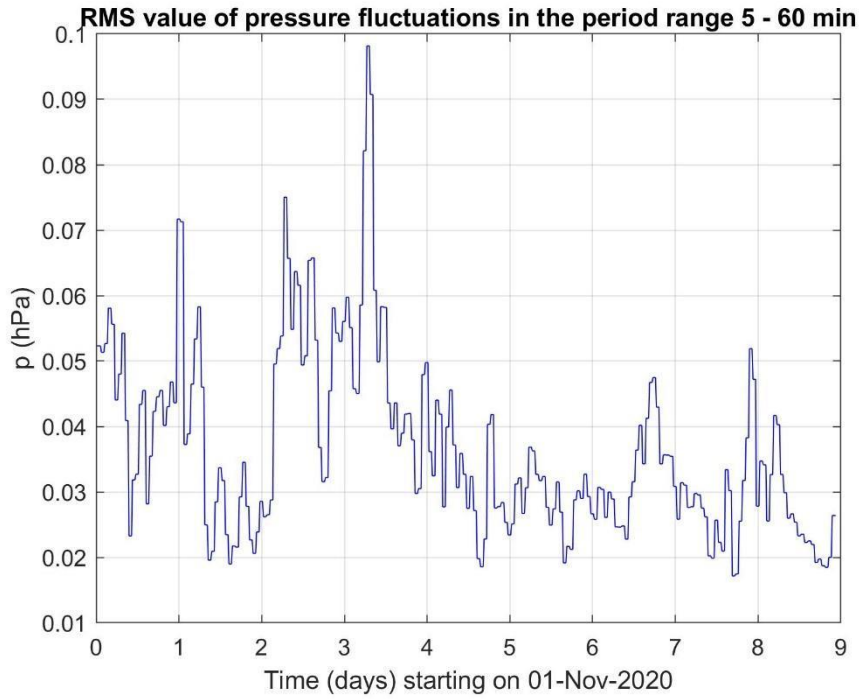
556 **3.2 Results and discussion of gravity waves in the troposphere and ionosphere**

557

558 **3.2.1 Investigation of GWs measured on the ground by WBCI array of micro-** 559 **barometers.**

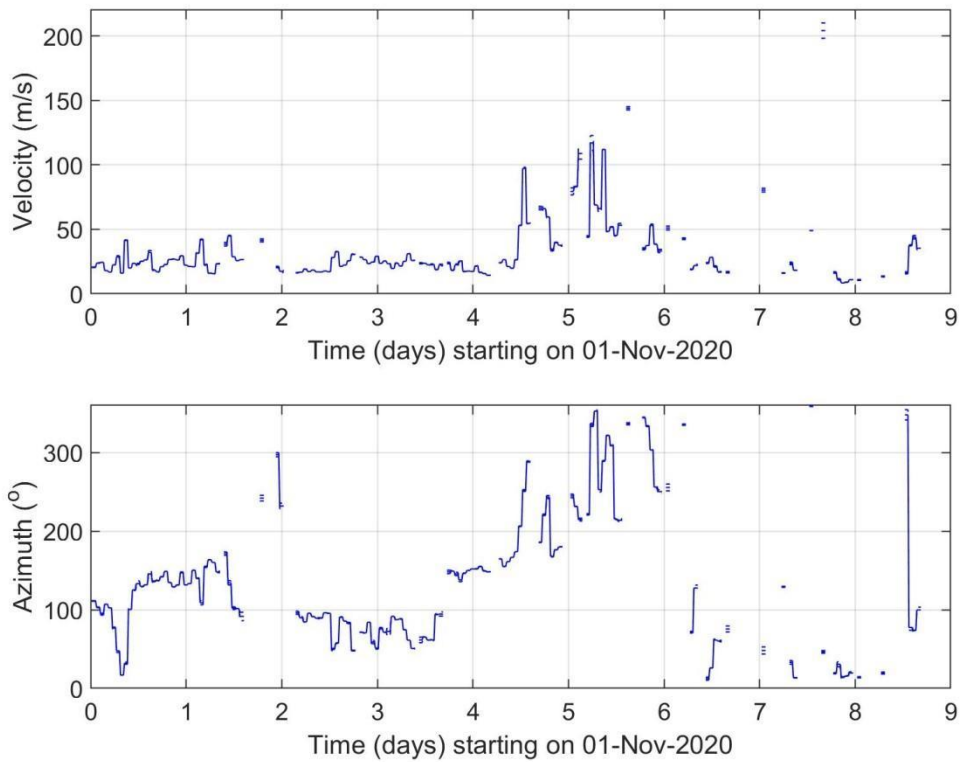
560 Figure 11 shows the RMS amplitudes of pressure fluctuations in the period range 5-60 min
561 recorded from November 1 to November 9, 2020. This interval covers a distinct streamer
562 event that occurred from November 3 to November 7. The results of propagation analysis are
563 shown in Figure 12, which displays the phase velocities and azimuths of GWs. Only results
564 that satisfied the criterion ($dv/v < 0.5$) and ($dAZ < 10^\circ$) and ($p_{RMS} > 0.02$ Pa) are presented,
565 where dv/v , dAZ , p_{RMS} are the relative uncertainty of GW phase velocity, uncertainty of
566 azimuth and root mean square value of pressure fluctuations in the analyzed time interval.
567 Figure 12 demonstrates that there is a tendency for higher phase velocities and occurrence of
568 different azimuths during the streamer event. Therefore, it is useful to compare the GW
569 characteristics during streamer events and calm conditions.

570 Figure 13 shows histograms obtained by a statistical analysis. The RMS amplitudes of
571 pressure fluctuations in the period range 5 – 60 min, phase velocities and azimuths were
572 investigated separately for calm conditions (upper plots) and for streamer events listed in
573 Table 1 (bottom plots) with a 1-hour time resolution. The solid vertical lines mark lower ($Q1$)
574 and upper ($Q3$) quartiles. The dashed vertical lines depict boundaries for large ($Q3 + 1.5 \cdot (Q3 -$
575 $Q1)$) and extreme ($Q3 + 3 \cdot (Q3 - Q1)$) values. A difference between histograms for RMS
576 pressure fluctuations and azimuths obtained for calm and disturbed conditions is obvious.
577 During the streamer events the azimuths are distributed more randomly and more extreme
578 pressure amplitudes can be observed. A minor difference is also observed for phase
579 velocities.



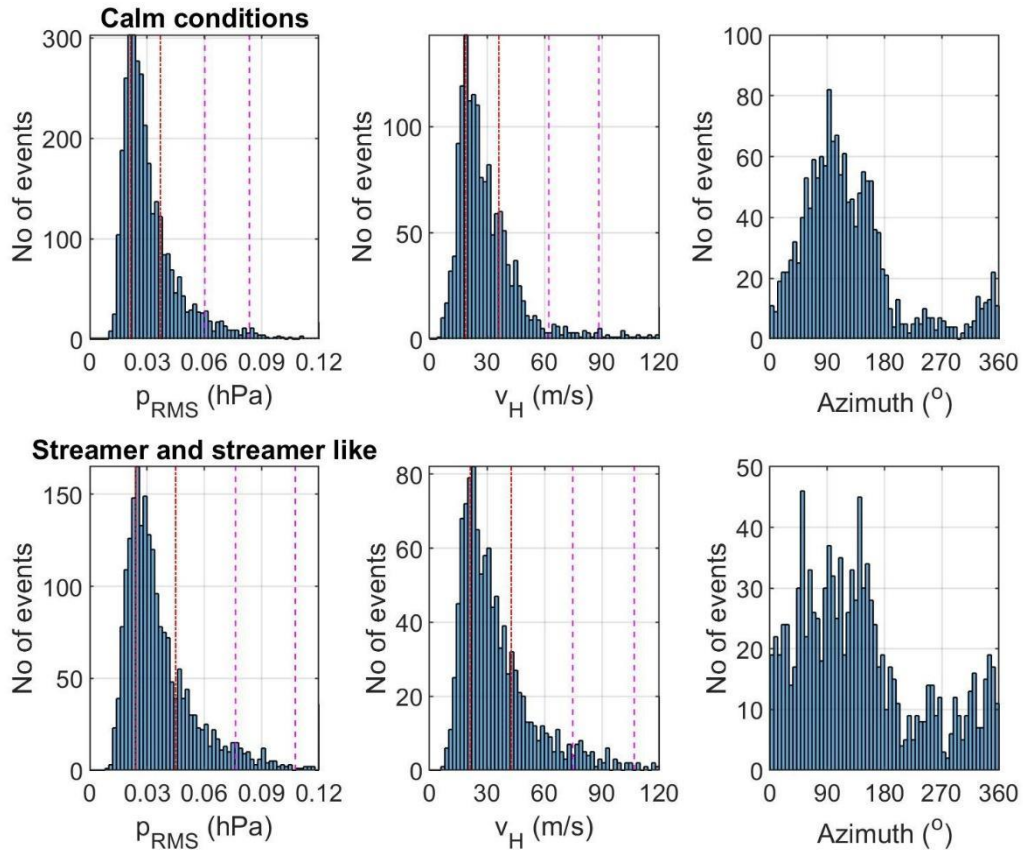
580

581 **Figure 11** Amplitude of GWs recorded by WBCI from 2020-11-01 to 2020-11-09



582

583 **Figure 12** Propagation velocity and azimuth of GWs recorded by WBCI from 2020-11-01 to
 584 2020-11-09



585

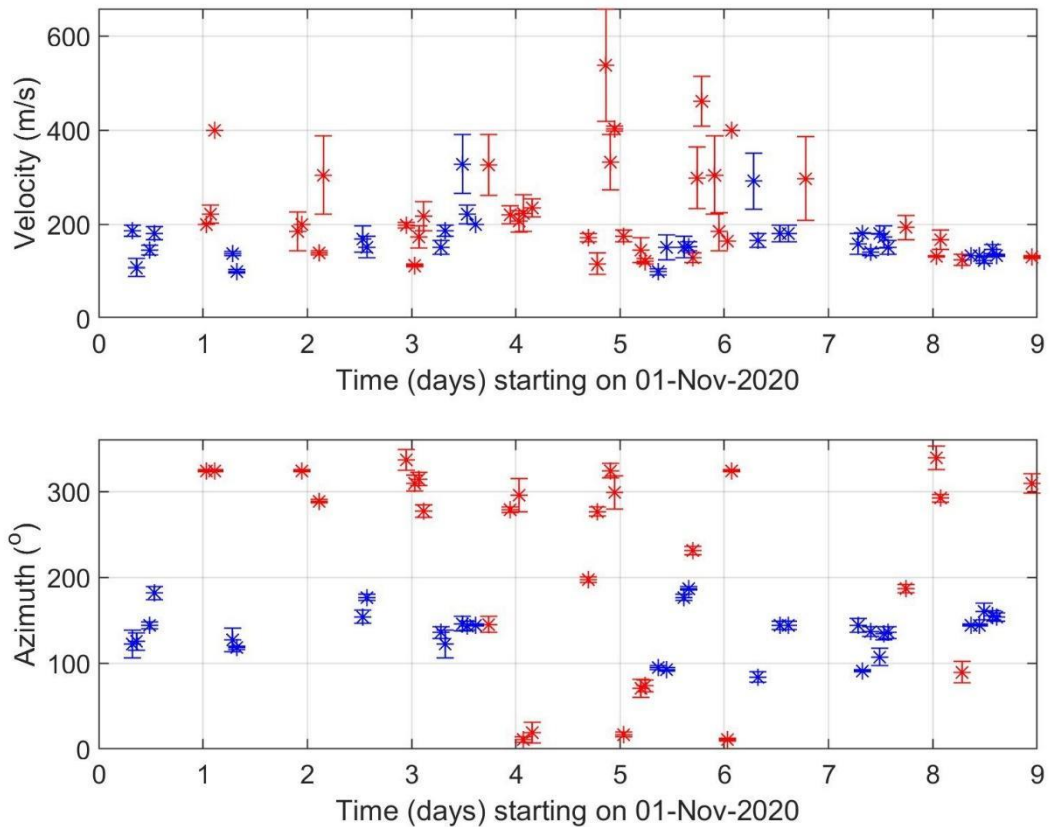
586 **Figure 13** GW characteristics (RMS of pressure fluctuations, phase velocity and azimuth)
 587 for calm periods (upper plots) and streamer and streamer like events (bottom plots) for 2020
 588 and winter 2021. The red vertical lines mark lower (Q1) and upper (Q3) quartiles. The dashed
 589 magenta vertical lines depict boundaries for large ($Q3 + 1.5 \cdot (Q3 - Q1)$) and extreme ($Q3 + 3 \cdot (Q3 -$
 590 $Q1)$) values.

591

592 3.2.2 Investigation of GWs measured in the ionosphere by continuous Doppler 593 sounding system (CDS)

594 The 2D propagation analysis of GWs was performed using the 2D versions of methods
 595 mentioned in Section 2 and in detail described by Chum and Podolska (2018). As discussed in
 596 Section 2 and by (Chum et al., 2021), the 2D propagation analysis makes it possible to
 597 analyze much larger number of time intervals than the 3D analysis. The propagation analysis
 598 obtained for the interval from 1st November to 9th November 2020, which covers the
 599 significant streamer event that occurred from 3rd November 2020 to 7th November 2020, is
 600 presented in Figure 14. Only results that satisfied the criteria ($dv/v < 0.2$) and ($dAZ < 20^\circ$) and

601 ($f_{\text{DRMS}} > 0.05$ Hz) and ($C_{\text{max}} < 0.5$) are presented, where dv/v is the relative uncertainty of GW
602 phase velocity, dAZ is the azimuth uncertainty, f_{DRMS} is the root mean square of the Doppler
603 shift in the analysed time interval and C_{max} is the maximum in the normalized energy map for
604 the best beam (slowness) search; C_{max} is 1 for identical signals (Chum and Podolská, 2018). It
605 is considered that signals are not sufficiently correlated (coherent) for reliable propagation
606 analysis if $C_{\text{max}} < 0.5$ (Chum et al., 2021). The velocities and azimuth obtained by observation
607 at 3.59 MHz are in red, whereas the values based on measurements at 4.65 MHz are in blue.
608 Obviously, the observations at 3.59 MHz mostly correspond to the nighttime, whereas
609 observations at 4.65 MHz were mostly made during the daytime. The 4.65 MHz signal did not
610 reflect from the ionosphere (escaped to the outer space) at night due to the low critical
611 frequency of the ionosphere. On the other hand, the 3.59 MHz signal mostly reflected during
612 the day from the ionospheric E layer and the Doppler shift was negligible, difficult to analyze.
613 The GWs usually propagated roughly poleward at night and roughly equatorward during the
614 daytime. This is fully consistent with the statistical investigation (Chum et al., 2021) which
615 showed that propagation directions of GWs in the ionosphere exhibit diurnal and seasonal
616 behavior and are mainly controlled by the neutral winds in the thermosphere.



617

618 **Figure 14** Propagation velocity and azimuth of GWs in the ionosphere obtained using CDS
619 measurements from 2020-11-01 to 2020-11-09. The velocities and azimuth obtained by
620 observation at 3.59 MHz are by red, whereas the values based on measurements at 4.65 MHz
621 are by blue.

622 Based on the analysis of the GW observed in the ionosphere during the streamer event and
623 on the previous statistical analysis, we conclude that no obvious signature related to streamer
624 event was observed for the propagation of GW the ionosphere.

625 It should be also mentioned that the phase velocities of GW measured on the ground (Figure
626 8) and at heights around 200 km in the ionosphere differ. There are several reasons for that.
627 First, the observed horizontal phase velocities depend on the elevation angle of GW
628 propagation and on the ambient temperature as follows from the dispersion relation (the
629 temperature enters the dispersion relation via the buoyancy frequency and the scale height).
630 The temperature in the ionosphere/thermosphere is several times higher than in the
631 troposphere. The elevation angles might change during the upward propagation of GWs,
632 depending on the wind and temperature profile. Second, GWs propagate with a tilt, not
633 vertically upward. It is therefore highly probable that the sources of the GWs observed in the
634 troposphere and ionosphere are different. Moreover, GW can break during their propagation
635 upward and secondary gravity waves might be observed in the ionosphere.

636 **4) Conclusion and discussion**

637 The focus of this study was to test independent types of observations like Doppler sounding
638 and microbarograph measurements for an analysis of GW behavior during streamer events,
639 which are strongly connected with PW or GW and the large scale mass transport of ozone and
640 that is why it can be very interesting for studies of atmospheric dynamics.

641 We also investigated infrasound propagation during streamer events, since modifications of
642 infrasound ducting in the atmosphere can be expected in these periods. We evaluated
643 infrasound detections at two microbarograph arrays in Central Europe during streamer events
644 and compared them with observation during adjacent quiet periods. To obtain an overview of
645 infrasound propagation from the source region to the region of observations, InfraGA/GeoAc
646 raytracing tools (Blom and Waxler, 2012; Blom, 2019) were employed. In general, geometric
647 acoustic approximation (raytracing) and the full wave models are used for simulations of
648 infrasound propagation through the atmosphere. The great advantage of the full wave models
649 is that they capture the leaking of energy between the waveguides. Waxler and Assink (2019)

650 emphasize particularly energy leaking between the tropospheric and stratospheric waveguide.
651 Geometrical acoustics approximation provides an easy-to-interpret model of infrasound
652 propagation in the atmosphere at lower computational costs compared to the full wave
653 models. Its disadvantage is that the geometrical acoustics approximation assumes no energy
654 propagation in the forbidden regions (for details see e.g. Waxler and Assink, 2019) and thus
655 provides a model of infrasound propagation in separated waveguides. Available methods of
656 infrasound propagation simulations are in detail discussed by Waxler and Assink (2019). The
657 approximation of atmospheric wave ducts provided by the raytracing was sufficient for the
658 purpose of our study; we aimed to obtain an elemental picture of infrasound propagation
659 during the periods of interest; it means to identify which wave guides are formed, their
660 directivity, and spatial extent.

661 The InfraGA/GeoAc predicts that a waveguide develops at the tropopause during the
662 analyzed streamer events in November 2020 and in March 2021 the direction of which is
663 determined by the disturbed jet-stream. The tropopause waveguide ducts infrasound up to
664 distances of several hundreds to a thousand of km from the source in a limited azimuth range.
665 The azimuth sector of the extent of $50 - 60^\circ$ is influenced in the analysed cases.

666 In accord with the model predictions, phenomena that can be unambiguously attributed to
667 streamer event effects were not found in infrasound detections at the infrasound stations PVICI
668 and WBCI during the studied cases. We assume that the observability of streamer event
669 signatures in infrasound arrival parameters depends on the mutual position of the source, the
670 streamer event disturbance of the tropopause jet-stream and the infrasound station. It can be
671 recommended for future studies to use a dense network of infrasound arrays that covers
672 various directions and distances from the streamer event. Due to the typical occurrence of the
673 streamer events over the North Atlantic, infrasound stations in Western Europe are of
674 particular interest.

675 Supplementary ground-based measurements of GW using the WBCI array in the troposphere
676 showed that GW propagation azimuths were more random during streamer and streamer-like
677 events compared to those observed during calm conditions as can be seen from the plots in
678 Figure 13. On the other hand, the GW propagation characteristics observed in the ionosphere
679 by CDS during streamer events did not differ from those expected for the given time period,
680 based on previous statistical studies (Chum et al., 2021).

681 The results therefore indicate that streamers in the stratosphere might lead to changes in wave
682 propagation in the troposphere. The impact on the ionosphere was not confirmed, but cannot

683 be excluded due to sparse and localized observations of GW activity. In general, to validate the
684 preliminary results obtained in this study, a denser measurement network and more streamer
685 events need to be analyzed.

686

687 **Data availability:**

688 ozone column measurements (TCO) which are available as a service by DLR at

689 <https://atmos.eoc.dlr.de/>

690 Ground to space model vertical atmospheric profiles were obtained at

691 <https://g2s.ncpa.olemiss.edu/>; accessed on 27 January – 4 February 2024

692

693 The WAVEWATCHIII[®] wave-action model data were accessed via ftp at
694 [polar.ncep.noaa.gov/waves/JCOMM/2020](ftp://polar.ncep.noaa.gov/waves/JCOMM/2020) on 13-14 March 2023.

695

696 The Deutscher Wetterdienst synoptic charts were accessed at

697 https://www2.wetter3.de/archiv_dwd_dt.html on 3 February 2024.

698

699 **Author contributions**

700 MK and LK create the idea of manuscript; JCh, MK, TS, LK, and KP suggest the datasets and
701 methods; TS, JCh, LK, KP and FT analyzed the data; MK wrote the manuscript draft; JCh,
702 TS, LK and KP reviewed and edited the manuscript.

703 **Competing interests**

704 The authors declare that they have no conflict of interest.

705

706 **Acknowledgement**

707 The DTK-GPMCC software was kindly provided by Commissariat à l'énergie atomique et
708 aux énergies alternatives, Centre DAM-Île-de-France, Département Analyse, Surveillance,
709 Environnement, Bruyères-le-Châtel, F91297 Arpajon, France.

710 The authors are grateful to Dr. Phil Blom and Los Alamos National Laboratory for opening
711 the InfraGA/GeoAc tools to the public.

712 We also acknowledge earth.nullschool.net for providing the figures.

713 **Financial support:** This study is supported by LISA project- Lidar measurements to
714 Identify Streamers and analyze Atmospheric waves, AEOLUS-INNOVATION, Contract No.
715 4000133567/20/I-BG

716

717 **References**

718 Assink, J.D., Waxler, R., Smets, P., Evers, L.G. (2014). Bidirectional infrasonic ducts
719 associated with sudden stratospheric warm-ing events. *J. Geophys. Res. Atmos.* 119,1140-
720 1153.

721 Bittner, M., Höppner, K., Pilger, C., Schmidt, C. (2010). Mesopause temperature
722 perturbations caused by infrasonic waves as a potential indicator for the detection of
723 tsunamis and other geo-hazards. *Nat. Hazards Earth Syst. Sci.*, 10, 1431-1442. [www.nat-](http://www.nat-hazards-earth-syst-sci.net/10/1431/2010/doi:10.5194/nhess-10-1431-2010)
724 [hazards-earth-syst-sci.net/10/1431/2010/doi:10.5194/nhess-10-1431-2010](http://www.nat-hazards-earth-syst-sci.net/10/1431/2010/doi:10.5194/nhess-10-1431-2010)

725 Blanc, E. (1985). Observations in the upper atmosphere of infrasonic waves from natural or
726 artificial sources: A summary. *Ann. Geophys.*, 3, 673-688.

727 Blixt, E.M., Nasholm, S.P., Gibbons, S.J., Evers, L.G., Charlton-Perez, A.J., Orsolini, Y.J.,
728 Kvaerna, T. (2019). Estimating tropo-spheric and stratospheric winds using infrasound from
729 explosions. *J. Acoust. Soc. Am.* 146:2.

730 Blom, P., Waxler, R. (2012). “Impulse propagation in the nocturnal boundary layer: Analysis
731 of the geometric component”. *J. Acoust. Soc. Am.*, **131**, 3680 – 3690. doi:
732 [10.1121/1.3699174](https://doi.org/10.1121/1.3699174).

733 Blom, P. (2019). “Modeling infrasonic propagation through a spherical atmospheric layer:
734 Analysis of the stratospheric pair.” *J. Acoust. Soc. Am.*, **145**, 2198–2208. doi:
735 [10.1121/1.5096855](https://doi.org/10.1121/1.5096855).

736 Bondár I., T. Šindelářová, D. Ghica, U. Mitterbauer, A. Liashchuk, J. Baše, J. Chum, C.
737 Czanik, C. Ionescu, C. Neagoe, M. Pásztor, A. Le Pichon (2022), Central and Eastern
738 European Infrasound Network: Contribution to Infrasound Monitoring, *Geophys. J. Int.*,
739 ggac066, <https://doi.org/10.1093/gji/ggac066>

740 Brachet, N., Brown, D., Le Bras R., Cansi, Y., Mialle, P., Coyne, J. (2010). Monitoring the
741 Earth's Atmosphere with the Global IMS Infrasound Network. In: Le Pichon, A., Blanc, E.,
742 Hauchecorne A. (Eds.), *Infrasound Monitoring for Atmospheric Studies*. Springer
743 Science+Business Media B.V., 77-118. Doi: 10.1007/978-1-4020-9508-5_3

744 Campus, P., Christie, D.R. (2010). Worldwide Observations of Infrasonic Waves. In: Le
745 Pichon, A., Blanc, E., Hauchecorne A. (Eds.), *Infrasound Monitoring for Atmospheric*
746 *Studies*. Springer Science+Business Media B.V., 185234-118. Doi: 10.1007/978-1-4020-
747 9508-5_6

748 Cansi, Y., 1995. An automatic seismic event processing for detection and location: The
749 P.M.C.C. method. *Geophys. Res. Lett.* 22, 1021-1024. doi: 10.1029/95GL00468

750 Ceranna, L., Matoza, R., Hupe, P., Le Pichon, A., Landès, M., (2019). Systematic Array
751 Processing of a Decade of Global IMS Infrasound Data. In: Le Pichon, A., Blanc, E.,
752 Hauchecorne, A. (eds) *Infrasound Monitoring for Atmospheric Studies. Challenges in*
753 *Middle Atmospheric Dynamics and Societal Benefits*. Springer Nature Switzerland AG.

754 Chum J, Podolská K (2018) 3D analysis of GW propagation in the ionosphere. *Geophysical*
755 *Research Letters*, 45, 11,562–11,571, <https://doi.org/10.1029/2018GL07969>

756 Chum, J., Podolská, K., Ruzs, J., Baše, J., Tedoradze, N. (2021), Statistical investigation of
757 gravity wave characteristics in the ionosphere. *Earth Planets Space* 73, 60,
758 <https://doi.org/10.1186/s40623-021-01379-3>

759 Czech microbarograph network, <https://doi.org/10.7914/SN/C9>

760 Drob, D. P., Picone, J. M., Garcés, M. (2003). Global morphology of infrasound propagation.
761 *J. Geophys. Res. Atmospheres*, **108** (D21). doi: [10.1029/2002JD003307](https://doi.org/10.1029/2002JD003307).

762 Evers, L. G., Siegmund, P. (2009). Infrasonic signature of the 2009 major sudden
763 stratosphericwarming, *Geophys. Res. Lett.*, 36, L23808, doi:10.1029/2009GL041323

764 Evers, L.G., Haak, H.W. (2010). The Characteristics of Infrasound, its Propagation and Some
765 Early History. In: Le Pichon, A., Blanc, E., Hauchecorne, A. (eds) *Infrasound Monitoring for*
766 *Atmospheric Studies*. Springer, Dordrecht.

767 Evers, L. G., van Geyt, A. R. J. , Smets, P., Fricke, J.T. (2012). Anomalous infrasound
768 propagation in a hot stratosphere and the existence of extremely small shadow zones, *J.*
769 *Geophys. Res.*, 117, D06120, doi:10.1029/2011JD017014.
770

771 Eyring, V., Dameris, M., Grewe, V., Langbein, I., & Kouker, W. (2002). Climatologies of
772 streamer events derived from a transport model and a coupled chemistry-climate model.

773 Fritts, D.C. & Alexander, M.J., (2003). Gravity wave dynamics and effects in the middle
774 atmosphere. *Rev. Geophys.*, 41 (1), 1003.

775 Garcès, M., Willis, M., Hetzer, C., Le Pichon , A., Drob, D., (2004). On using ocean swells
776 for continuous infrasonic measurements of winds and temperature in the lower, middle, and
777 upper atmosphere. *Geophys. Res. Lett.* 31, L19304. doi: 10.1029/2004GL020696

778 Garcès, M.A., (2013). On infrasound standards, part 1: Time, frequency, and energy scaling.
779 *InfraMatics* 2, 13-35. doi: 10.4236/inframatics.2013.22002

780 Georges, T.M. (1968). H. F. Doppler studies of travelling ionospheric disturbances. *J.*
781 *Atmos.Terr. Phys.*, 30, 735-746.

782 Gerlach, C., Földvary, L., Švehla, D., Gruber, T., Wermuth, M., Sneeuw, N., ... &
783 Steigenberger, P. (2003). A CHAMP-only gravity field model from kinematic orbits using the
784 energy integral. *Geophysical Research Letters*, 30(20).

785 Hersbach, H., Bell, B., Berrisford, P., Hirahara, S., Horányi, A., Muñoz-Sabater, J., ... &
786 Thépaut, J. N. (2020). The ERA5 global reanalysis. *Quarterly Journal of the Royal*
787 *Meteorological Society*, 146(730), 1999-2049.

788 Hupe, P., Ceranna, L., Pilger, C., de Carlo, M., Le Pichon, A., Kaifler, B., Rapp, M. (2019).
789 Assessing middle atmosphere weather models using infrasound detections from microbaroms.
790 *Geophys. J. Int.*, 216, 1761–1767 doi: 10.1093/gji/ggy520

791 James, P. M. (1998): A climatology of ozone mini-holes over the Northern Hemisphere.
792 *International Journal of Climatology: A Journal of the Royal Meteorological Society*, 18, 12:
793 12871303

794 Kramer, R, S. Wüst, and M. Bittner (2016). Investigation of gravity wave activity based on
795 operational radiosonde data from 13 years (1997-2009): Climatology and possible induced
796 variability, *Journal of Atmospheric and Solar-Terrestrial Physics* 140, 23–33;
797 <http://dx.doi.org/10.1016/j.jastp.2016.01.014>

798 Kramer, R., S. Wüst, C. Schmidt, and M. Bittner (2015). Gravity wave characteristics in the
799 middle atmosphere during the CESAR campaign at Palma de Mallorca in 2011/2012: Impact
800 of extratropical cyclones and cold fronts, *Journal of Atmospheric and Solar-Terrestrial*
801 *Physics* 128 (2015) 8–23, <http://dx.doi.org/10.1016/j.jastp.2015.03.001>

802 Kai Ming Huang, Shao Dong Zhang, Fan Yi, (2010). Reflection and transmission of
803 atmospheric gravity waves in a stably sheared horizontal wind field, *Journal of Geophysical*
804 *Research: Atmospheres*, 10.1029/2009JD012687, **115**, D16,

805 Landès, M., Ceranna, L., Le Pichon, A., & Matoza, R. S. (2012). Localization of microbarom
806 sources using the IMS infrasound network. *Journal of Geophysical Research:*
807 *Atmospheres*, 117(D6).

808 Le Pichon, A., Cansi, Y. (2003). PMCC for infrasound data processing. *InfraMatics* 02, 1-9.

809 Le Pichon, A., Blanc, E., (2005). Probing high-altitude winds using infrasound. *J. Geophys.*
810 *Res.*, 110, D20104. doi: 10.1029/2005JD006020

811 Le Pichon, A., Ceranna, L., Garcès, M., Drob, D., Millet, C., (2006). On using infrasound
812 from interacting ocean swells for global continuous measurements of winds and temperature
813 in the stratosphere. *J. Geophys. Res.*, 111, D11106. doi: 10.1029/2005JD006690

814 Le Pichon, A., Vergoz, J., Blanc, E., Guilbert, J., Ceranna, L., Evers, L., Brachet, N., (2009).
815 Assessing the performance of the International Monitoring System's infrasound network:
816 Geographical coverage and temporal variabilities. *J. Geophys. Res.* 114, D08112. doi:
817 10.1029/2008JD010907

818 Leovy, C. B., Sun, C. R., Hitchman, M. H., Remsberg, E. E., Russell III, J. M., Gordley, L.
819 L., ... & Lyjak, L. V. (1985). Transport of ozone in the middle stratosphere: Evidence for
820 planetary wave breaking. *Journal of Atmospheric Sciences*, 42(3), 230-244.

821 Lonzaga, J.B., (2015). A theoretical relation between the celerity and trace velocity of
822 infrasonic phases, *J. Acoust. Soc. Am.*, 138, EL242-EL247.
823 <http://dx.doi.org/10.1121/1.4929628>

824 Loyola D.G., Koukouli M.E., Valks P., Balis D.S., Hao N., van Roozendaal M., Spurr R.J.D.,
825 Zimmer W., Kiemle S., Lerot C., Lambert J.-C. (2011) The GOME-2 total column ozone
826 product: Retrieval algorithm and ground-based validation, *Journal of Geophysical Research*,
827 vol. 116, D07302, Wiley-Blackwell

828 Marty, J., (2019). The IMS Infrasound Network: Current Status and Technological
829 Developments, in: Le Pichon, A., Blanc, E., Hauchecorn, A. (Eds.), *Infrasound Monitoring*
830 *for Atmospheric Studies. Challenges in Middle Atmosphere Dynamics and Societal Benefits*.
831 Springer Nature Switzerland AG, pp. 3–62. doi:10.1007/978-3-319-75140-5_1

832 McIntyre, M. E., & Palmer, T. N. (1983). Breaking planetary waves in the stratosphere.
833 *Nature*, 305(5935), 593-600.

834 Munro, R., Eisinger, M., Anderson, C., Callies, J., Corpaccioli, E., Lang, R., ... & Albinana,
835 A. P. (2006, June). GOME-2 on MetOp. In *Proc. of The 2006 EUMETSAT Meteorological*
836 *Satellite Conference*, Helsinki, Finland (Vol. 1216, p. 48).

837 Munro, R., et al. (2016): The GOME-2 instrument on the Metop series of satellites:
838 instrument design, calibration, and level 1 data processing – an overview, *Atmos. Meas.*
839 *Tech.*, 9, 1279–1301, <https://doi.org/10.5194/amt-9-1279-2016>.

840 Peters, D., Hoffmann, P., & Alpers, M. (2003). On the appearance of inertia-gravity waves on
841 the north-easterly side of an anticyclone. *Meteorologische Zeitschrift*, 12(1), 25-35

842 Polvani, L. M., & Plumb, R. A. (1992). Rossby wave breaking, microbreaking, filamentation,
843 and secondary vortex formation: The dynamics of a perturbed vortex. *Journal of Atmospheric*
844 *Sciences*, 49(6), 462-476.

845 Pramitha, M., Venkat Ratnam, M., Taori, A., Krishna Murthy, B. V., Pallamraju, D., and
846 Vijaya Bhaskar Rao, S. (2015). Evidence for tropospheric wind shear excitation of high-
847 phase-speed gravity waves reaching the mesosphere using the ray-tracing technique, *Atmos.*
848 *Chem. Phys.*, 15, 2709–2721, <https://doi.org/10.5194/acp-15-2709-2015>.

849 Rauthe, M., Gerding, M., Höffner, J., & Lübken, F. J. (2006). Lidar temperature
850 measurements of gravity waves over Kühlungsborn (54° N) from 1 to 105 km: A winter-
851 summer comparison. *Journal of Geophysical Research: Atmospheres*, 111(D24).
852

853 Wüst, S., & Bittner, M. (2006). Non-linear resonant wave–wave interaction (triad): Case
854 studies based on rocket data and first application to satellite data. *Journal of atmospheric and*
855 *solar-terrestrial physics*, 68(9), 959-976.
856

857 Wüst, S., Offenwanger, T., Schmidt, C., Bittner, M., Jacobi, C., Stober, G., Yee, J.H.,
858 Mlynczak, M. G. & Russell III, J. M. (2018). Derivation of gravity wave intrinsic parameters
859 and vertical wavelength using a single scanning OH (3-1) airglow spectrometer. *Atmospheric*
860 *Measurement Techniques*, 11(5), 2937-2947.
861

862 Smets, P.S.M., Evers, L.G. (2014). The life cycle of a sudden stratospheric warming from
863 infrasonic ambient noise observations, *J. Geophys. Res. Atmos.*, 119, 12,084-12,099

864 Spurr, R., Loyola, D., Heue, K. P., Van Roozendael, M., & Lerot, C. (2022). S5P/TROPOMI
865 Total Ozone ATBD. Deutsches Zentrum für Luft- und Raumfahrt (German Aerospace
866 Center), Weßling, Germany, Tech. Rep. S5P-L2-DLR-ATBD-400A.

867 Sutherland, L.C., Bass, H.E., (2004). Atmospheric absorption in the atmosphere up to 160
868 km. *J. Acoust. Soc. Am.*, 115, 1012–1032. <https://doi.org/10.1121/1.1631937>

869 Szuberla, C.A.L., Olson, J.V., (2004). Uncertainties associated with parameter estimation in
870 atmospheric infrasound rays. *J. Acoust. Soc. Am.* 115, 253-258. doi: 10.1121/1.1635407

871 Veefkind, J. P., Aben, I., McMullan, K., Förster, H., De Vries, J., Otter, G., ... & Levelt, P. F.
872 (2012). TROPOMI on the ESA Sentinel-5 Precursor: A GMES mission for global
873 observations of the atmospheric composition for climate, air quality and ozone layer
874 applications. *Remote sensing of environment*, 120, 70-83.

875 Waxler, R., Assink, J., 2019. Propagation Modeling Through Realistic Atmosphere and
876 Benchmarking, in: Le Pichon, A., Blanc, E., Hauchecorn, A. (Eds.), *Infrasound Monitoring*
877 *for Atmospheric Studies. Challenges in Middle Atmosphere Dynamics and Societal Benefits.*
878 Springer Nature Switzerland AG, pp. 3–62. doi:10.1007/978-3-319-75140-5_15
879
880